Journal of Marine Science and Application (2026) 25: 15-31
https://doi.org/10.1007/s11804-025-00622-7

RESEARCH ARTICLE

Numerical Study on the Correlation Between Underwater Radiated Noise and Wake Evolution of a Rim-Driven Thruster

Jie Gong[1,2,3] and Zhongwan Wu[1,2,3]

Received: 24 September 2024 / Accepted: 16 January 2025

Abstract

In this investigation, a hybrid approach integrating the IDDES turbulence model and FW-H is employed to forecast the hydroacoustic of the rim-driven thruster (RDT) under non-cavitation and uniform flow conditions at varying loading conditions (J = 0.3 and J = 0.6). It is revealed that the quadrupole term contribution in the P-FWH method significantly affects the monopole term in the low-frequency region, while it mainly affects the dipole term in the high-frequency region. Specifically, the overall sound pressure levels (SPL) of the RDT using the P-FWH method are 2.27 dB, 10.03 dB, and 16.73 dB at the receiving points from R1 to R3 under the heavy-loaded condition, while they increase by 0.67 dB at R1, and decrease by 14.93 dB at R2, and 22.20 dB at R3, for the light-loaded condition. The study also utilizes the pressure-time derivatives to visualize the numerical noise and to pinpoint the dynamics of the vortex cores, and the optimization of the grid design can significantly reduce the numerical noise. The computational accuracy of the P-FWH method can meet the noise requirements for the preliminary design of rim-driven thrusters.

Keywords Rim-driven thruster; Hydrodynamics; Underwater radiated noise; Non-cavitation; Numerical noise

1 Introduction

Ship noise sources are primarily classified into three categories: mechanical noise, propeller noise, and hydrodynamic noise (ITTC, 2014a). It is widely acknowledged that propeller noise represents the primary source of noise for ship operations (Cruz et al., 2022; Transport Canada/Government of Canada, 2019). Its radiated noise frequency range overlaps with the vocal and auditory frequency ranges of numerous marine animals, which can have a profound negative impact on marine life (Duarte et al., 2021; Sørensen et al., 2023). Furthermore, the exposed paddle blades are prone to cause harm to marine fish and scouring hazards to the shallow seabed of near-island reefs. To address the adverse impacts of ship propulsion systems on marine life and the environment, it is necessary to implement measures to mitigate these effects. Meanwhile, the development of large-scale ships has led to the emergence of large propulsion shaft systems, which have resulted in several challenges, including the occupation of large space, complex structures, energy transfer loss, and increased difficulty in ship design and construction costs. In response, there has been a shift in focus towards the research and development of special propulsion devices (Andersen and Andersen, 1987; Gaggero et al., 2016a, 2016b). In the context described above, the rim-driven thruster (RDT) represents a superior alternative. However, the complexity of its structure, the existence of conflicting design criteria, and the engineering challenges it presents have hitherto constrained its performance. The advent of recent technological advances has now made the RDT a viable proposition (Yan et al., 2017). It comprises a permanent magnet rotor mounted on the rim, integrating the motor rotor and blades into a single unit (Abu Sharkh et al., 2003). This eliminates the propeller blade leakage vortices and significantly reduces the vibration and noise caused by the thruster (Yan et al., 2017; Tan et al., 2015). Theoretically, the RDT exhib-

Article Highlights

- The rim-driven thruster (RDT) wake evolution is closely linked to noise radiation, and optimizing wake structure can effectively reduce noise levels.
- The RDT noise is up to 20 dB, lower than that of conventional propellers.
- Noise characteristics and optimization directions are identified, supporting the design of rim-driven thrusters.

✉ Zhongwan Wu
wzw719@whut.edu.cn

[1] Key Laboratory of High Performance Ship Technology (Wuhan University of Technology), Ministry of Education, Wuhan 430063, China

[2] Sanya Science and Education Innovation Park of Wuhan University of Technology, Sanya 572000, China

[3] School of Naval Architecture, Ocean and Energy Power Engineering, Wuhan University of Technology, Wuhan 430063, China

its several advantages, including high efficiency, anti-cavitation, low noise, and a compact structure. However, its unique structure and "rim effect" contribute to the complexity of the source of thruster noise. Consequently, this study focuses on underwater radiated noise (URN) concerning the RDT.

The prediction of the URN of propellers can be accomplished using numerical calculations, empirical formulas, and experimental measurements. Currently, the majority of scholars employ viscous or potential flow-based solvers in conjunction with acoustic analogy methods to numerically predict the URN of propellers. Among the numerous acoustic analog methods, the Ffowcs Williams-Hawkings (FW-H) method is particularly well-suited to consider the motion boundary, which is the most suitable for the noise problem of propellers (Ffowcs Williams and Hawkings, 1969). Consequently, the majority of scholars have employed the surface element method or a hybrid approach combining computational fluid dynamics (CFD) and FW-H to forecast the URN of propellers. The FW-H acoustic analogy method can be divided into two categories: direct FW-H (D-FWH), which integrates the three-dimensional body sources directly, and permeable FW-H (P-FWH), which calculates the envelope noise sources in a specific implementation. Due to the high computational cost of D-FWH, most scholars currently employ the P-FWH method to calculate the radiated noise of propellers. However, it has been recently demonstrated that the P-FWH method exhibits a numerical noise problem (Lidtke et al., 2019; Lloyda et al., 2015; Testa et al., 2021). Sezen et al. (2021a) conducted a study to assess the impact of grid resolution on the prediction of noise performance by the Reynolds-averaged Navier-Stokes equations (RANS) method. Their findings indicated that while increasing the mesh resolution could reduce the numerical noise generated by the slip intersection interface, it could not eliminate it entirely.

The majority of current studies are focused on the design and analysis of the RDT motor system (Hughes et al., 2000), with a particular emphasis on blade vibration-related issues (Chen et al., 2017). However, there is a paucity of studies investigating the hydrodynamic characteristics of the blade, particularly in relation to noise characteristics. In a previous study(Wu et al., 2023a, 2023b), a design scheme for an RDT with zero skew, zero rake, and a semi-elliptical projection profile with equal pitch was proposed. The design scheme employs a fusiform section, with a decompression factor (ξ) that is smaller than that of an airfoil section. This configuration is less prone to cavitation. Additionally, the incorporation of a permanent magnet motor and rim enhances the tip-loading and cavitation performance of the RDT (Lea et al., 2003). Consequently, this study is conducted under non-cavitation and homogeneous flow conditions. This study employs a hybrid method of Improved Delayed Detached Eddy (IDDES) and FW-H to investigate the hydrodynamic characteristics of the RDT. Additionally, a comparison between the RDT and a conventional propeller under identical operating conditions allows for a more intuitive understanding of the differences between the two. This comparison facilitates the identification of the specific characteristics that contribute to the noise profile of the RDT. Consequently, in this study, the INSEAN E779A propeller, a widely studied reference object, is selected for a comparative study on the noise characteristics of marine propellers.

2 Numerical modeling

2.1 Research object

The RDT is comprised of a duct, a rim, and a propeller, with the rim and propeller integrated into a single component, separated from the duct by a gap. In order to avoid any potential confusion with the established definition of a propeller, the same definition is utilized here. Based on the presence or absence of a hub at the hub area of the propeller, RDTs can be classified as either hubless or hub.

The object of this study is a five-bladed hubless RDT whose duct consists of a NACA2412 airfoil and whose blades consist of a fusiform airfoil with equal pitch, zero skew, and zero rake (Figure 1). Figure 1(a) illustrates the components of the RDT: the duct is white, the rim is brown, and the propeller (blade) is green. The RDT has a diameter of 0.25 m and a pitch ratio of P/D = 1.2. The conventional propeller reference for this study is the INSEAN E779A propeller, which has a diameter of 0.227 m and a pitch ratio of P/D = 1.11.

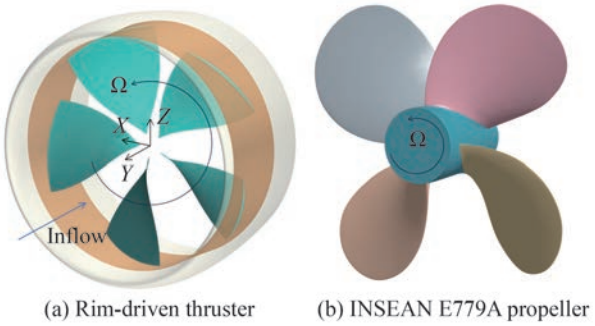

Figure 1 Rim-driven thruster and INSEAN E779A propeller

The discrepancy between the torque coefficient of the RDT designed in this study and that of the E779A propeller is 0.84% at J = 0.3, while the difference between the thrust coefficient of the RDT blade and that of the E779A propeller blade is 0.13% at J = 0.6. It can be assumed that the power required by the 5-bladed RDT is equivalent to that of the E779A propeller under the heavy-loaded condi-

tion, while the thrust generated by the RDT blade is equivalent to that of the E779A propeller under the light-loaded condition. Therefore, it is more reasonable to use the E779A propeller as the reference object of this study. This is also the reason why the number of RDT blades and the number of E779A propeller blades are different.

2.2 Control equations

2.2.1 Hydrodynamic model

In this study, a scale-resolved simulation DES method based on a two-equation SST $k-\omega$ turbulence model is employed to solve the flow field under incompressible conditions (Gong et al., 2023, 2021, 2018; Gaggero, 2023). Here, RANS is utilized for the attached boundary, while LES is applied to the large-scale separated regions to reduce the computational cost and capture anisotropic vortical structures (Spalart et al., 1997). The DES formulation of the SST $k-\omega$ model can be obtained by modifying the dissipation term in the turbulent kinetic energy transport Eq. (1). However, the traditional DES and DDES methods for conversion from RANS to LES positions are based on local mesh refinement, which usually leads to an error called log-layer mismatch (Sharma et al., 2019; Shur et al., 2008; Spalart, 2009). The IDDES can alleviate these problems. In this study, the dissipation rate ω in equation (1) is replaced by $\tilde{\omega}$, defined as follows, based on the IDDES formulation proposed by Shur et al. (Shur et al., 2008):

$$\frac{\partial}{\partial t}(\rho k) + \nabla \cdot (\rho k \bar{v}) = \nabla \cdot \left[(\mu + \sigma_k \mu_t)\nabla k\right] + P_k - \rho\beta^* f_{\beta^*}(\omega k - \omega_0 k_0) + S_k \tag{1}$$

$$\tilde{\omega} = \frac{\sqrt{k}}{l f_{\beta^*} \beta^*} \tag{2}$$

where $\bar{v}$ is the mean velocity, μ is the dynamical viscosity, σ_k and β^* are the model coefficients, P_k is the production term, f_{β^*} is the free-shear modification factor, S_k is the user-specified source term, and k_0 and ω_0 are the ambient turbulence values that counteract turbulence decay. l is defined as follows:

$$l = \tilde{f}_d(1 + f_e) l_{\mathrm{RANS}} + \left(1 - \tilde{f}_d\right) C_{\mathrm{DES}} \Delta_{\mathrm{IDDES}} \tag{3}$$

Two more functions are introduced to the length scale calculation to add Wall-Modeled LES (WMLES) capability, a blending function f_B and the elevating function f_e:

The IDDES model utilized in the current study constructs a unified set of formulas for both the DDES and WMLES. This new sub-grid length scale is dependent not only on the grid size but also on the wall-normal distance, thus eliminating the log-law mismatch error. In the RANS mode of the calculation, the SST $k-\omega$ model is employed to facilitate the simulation in instances where adverse pressure gradients are pronounced within the flow field (Wang et al., 2021).

2.2.2 Hydroacoustic model

In this study, the FW-H acoustic analogy methods are employed to predict the noise performance of the thruster. The P-FWH method defines an integral domain (i.e., a permeable surface) around the thruster, thereby ensuring that all relevant nonlinear contributions are included in the calculations to the greatest extent possible. In the P-FWH equations, the nonlinear terms within the integration domain are evaluated by solving the surface integral rather than the volume integral. Consequently, the monopole and dipole terms lose their physical significance in the impermeable method and become "pseudo-monopole" and "pseudo-dipole" terms that include quadrupole contributions. In the P-FWH equation, two new variables (U_n and L_i) are introduced as the modified velocity and modified stress tensor, respectively, defined as follows (Di Francescantonio, 1997; Farassat, 2007; Ge et al., 2022; Sezen and Atlar, 2023):

$$U_n = \left(1 - \frac{\rho}{\rho_0}\right) v_n + \frac{\rho}{\rho_0} u_n \tag{4}$$

$$L_i = p\delta_{ij} n_j + \rho u_i (u_n - v_n) \tag{5}$$

Therefore, when considering impermeable surfaces in motion, referred to as S-FWH:

$$\Box^2 p' = \frac{\partial}{\partial t}\left[\rho_0 v_n \delta(f)\right] - \frac{\partial}{\partial x_i}\left[p n_i \delta(f)\right] + \frac{\partial^2}{\partial x_i \partial x_j}\left[H(f) T_{ij}\right] \tag{6}$$

And when considering permeable surfaces in motion, referred to as P-FWH:

$$\Box^2 p' = \frac{\partial}{\partial t}\left[\rho_0 U_n\right]\delta(f) - \frac{\partial}{\partial x_i}\left[L_i \delta(f)\right] + \frac{\partial^2}{\partial x_i \partial x_j}\left[H(f) T_{ij}\right] \tag{7}$$

where $\Box^2$ is the D'Alembert operator, n is the unit outward normal of the surface, v_n is the local normal velocity of the surface, p is the local gage pressure on the surface, T_{ij} is the Lighthill stress tensor, δ_{ij} is the Dirac delta function, σ_{ij} is the viscous stress tensor, and $H(f)$ is the Heaviside function.

In Eq. (6) and (7), the first term on the right-hand side represents the linear thickness term, while the second term represents the linear loading term. Both terms are taken over the impermeable surface $f = 0$ via the Dirac delta

function $\delta(f)$. The third term, which includes the Heaviside function $H(f)$ and the Lighthill stress tensor T_{ij}, represents the nonlinear quadrupole term outside the surface $f = 0$. The P-FWH method eliminates the need for volume partitioning in the calculation of the nonlinear term, thereby reducing the computational cost significantly.

Brentner and Farassat (1998) have shown that the noise contribution from the quadrupole, can be expressed as a "collapsing-sphere" formulation. Accordingly, the "collapsing-sphere" method is employed in this study to pursue the volume integration of turbulent noise. The space derivatives from Eq. (8) are transformed into time derivatives in Eq. (9).

$$p'_Q(x,t) = \frac{1}{4\pi}\left(\left(\frac{\partial^2}{(\partial x_i)(\partial x_j)}\right)\int_v\left[\frac{T_{ij}}{(r(1-M_r))}\right]_{ret} \mathrm{d}V\right) \quad (8)$$

$$\begin{aligned} p'_Q(x,t) = {} & \frac{1}{4\pi}\left(\left(\frac{1}{c}\right)\left(\frac{\partial^2}{\partial t^2}\right)\int_{-\infty}^{t}\left[\int_{(f>0)}\frac{T_{rr}}{r}\mathrm{d}\Omega\right]\mathrm{d}\tau + \right. \\ & \left(\frac{\partial}{\partial t}\right)\int_{-\infty}^{t}\left[\int_{(f>0)}\frac{3T_{rr}-T_{ii}}{r^2}\mathrm{d}\Omega\right]\mathrm{d}\tau\Big) + \\ & \left.\left(c\int_{-\infty}^{t}\left[\int_{(f>0)}\frac{3T_{rr}-T_{ii}}{r^3}\mathrm{d}\Omega\right]\mathrm{d}\tau\right)\right. \end{aligned} \quad (9)$$

where T_{rr} is the double contraction of T_{ij}, r_i and r_i are the components of the unit vector in the direction of radiation, T_{ij} is the Lighthill stress tensor.

2.3 Numerical calculation details

2.3.1 Computational domain & Boundary conditions

First, the dimensionless coefficients of the thruster are elucidated. In the RDT, $10K_Q$ represents the torque coefficients of the blade and rim, K_{TP} represents the thrust coefficients of the blade, K_{TD} represents the thrust coefficients of the duct, and K_{TR} represents the thrust coefficients of the rim. Due to the simplification of the rim in this study, the blade and rim are expressed as a single entity in this paper, i.e., K_{TR} and K_{TP} are combined as K_{TP}. The hydrodynamic coefficient of the RDT with diameter D and speed n is defined as follows:

$$10K_Q = 10\cdot\frac{Q_P+Q_R}{\rho n^2 D^5}, K_{TP} = \frac{T_P+T_R}{\rho n^2 D^4}, K_{TD} = \frac{T_D}{\rho n^2 D^4} \quad (10)$$

A cylindrical computational domain, comprising a static outer domain and a rotating inner domain, was employed in the numerical calculations (Figure 2). The radius of the computational domain is 4D (thruster diameter), with a distance of 4D upstream from the thruster center and 8D downstream. The rotating domain transitions to the static domain through a slip interface, with boundary conditions for both the upstream inlet and far-field as velocity inlet, and for the downstream outlet as pressure outlet. To include as much of the associated nonlinear noise contributions as possible, the permeable data surface (PDS) is placed outside the interface region. In this study, the computational domain is delineated using a trimmed cell mesh, and a prism layer mesh is employed to simulate the flow in the wall boundary layer. The local mesh scale in this study employs refined volumes with varying isotropic sizes to capture the fundamental flow characteristics. The surface mesh size of the RDT is 0.001 m, i.e., 0.4%D. The rotating inner domain mesh size is 0.002 5 m, i.e., 1%D. The refined mesh size of the thruster and the near- and mid-tail wake regions is 0.002 5 m, i.e., 1%D. The unrefined mesh size of the mid- and far-tail wake regions is 0.005 m, i.e., 2%D. In this study, a constant rotational speed of n = 1 500 r/min is used, and different advance coefficients J $(J = U/(nD))$ are achieved by varying the velocity U. The fluid density (ρ) is 997.561 kg/m^3, and the Reynolds number (Re) is 5.3×10^5. Based on the final discretization of the mesh, the dimensionless rotational period (T) and time step (Δt) are set to $T = 2\pi$ and Δt = 2e−4, respectively.

In this study, the Fast Fourier Transform (FFT) method was employed to transform the time-domain data into frequency-domain data. Following the stabilization of the

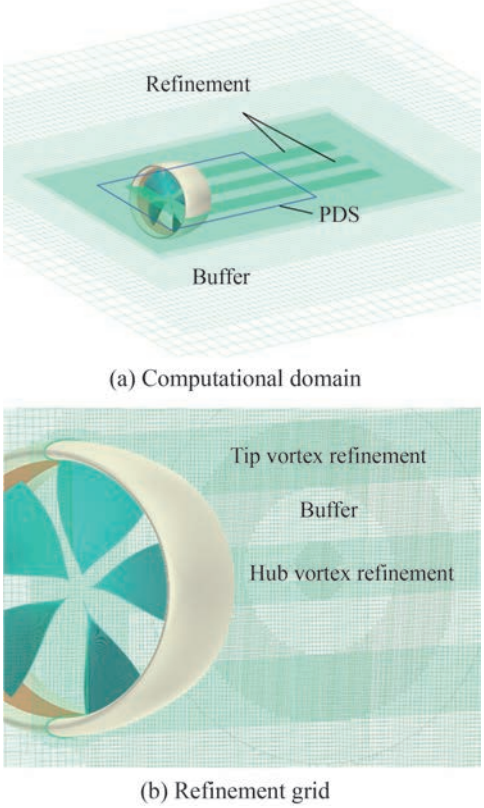

Figure 2 Computational domain grid

results, the acquisition duration was set to 1s, corresponding to a frequency resolution of Δf = 1 Hz. The converted data utilized the Hanning window function, and a Band pass filter was applied to the data in this study.

To perform the aforementioned computational process, this study employs the finite volume method with a separated flow solver, considers the rotational motions of the blade and rim using a rigid body motion model, and couples the pressure-velocity equations using the SIMPLE algorithm. Specifically, the convective and transient terms are discretized using the Hybrid-BCD format (which blends second-order upwind and bounded-central differencing) and the second-order implicit method, respectively, with an all y^+ wall treatment (Siemens, 2022). To satisfy the requirements of the IDDES algorithm, the y^+ value of the wall surface is restricted to $y^+ < 1$. In the IDDES simulations, the temporal and spatial scales are balanced according to the Courant-Friedrichs-Lewy number (CFL) recommendation of the ITTC (ITTC, 2014b). In this paper, each time-step in the numerical calculations corresponds to a rotational motion angle of less than 2°.

2.3.2 Numerical method validation and uncertainty analysis

To verify the accuracy and reliability of the numerical method, we conducted a comparison between the numerical method used in this study and the published test data and numerical calculations. It should be noted that the locations of the receiver point for forecasting the noise performance in this study are shown in Table 1 and the coordinate orientation is shown in Figure 1, and the locations of the receiver points are the same as those in the published studies (Ianniello et al., 2013; Sezen et al., 2021b).

This subsection examines the hydrodynamic performance of the INSEAN E779A propeller at J = 0.3, 0.6, 0.88, and n = 1 500 r/min. The results are compared with those obtained from experimental measurements (Table 2). The results of the numerical calculation of the thrust and torque coefficients of the E779A propeller in comparison to the test data indicate an error of 3.25% and 0.14%, respectively, at J = 0.3. At J = 0.6, the thrust coefficient error is 2.46% and the torque coefficient error is 1.80%. At J = 0.88, the thrust coefficient error is 5.29% and the torque coefficient error is 0.06%.

Table 1 Position of receiving points

Receiving points	X (m)	Y (m)	Z (m)
R1	0	0.140 3	0.264 8
R2	0	0	0.264 8
R3	0	−0.127 9	0.264 8

Table 2 Numerical results using a reference grid

	4-bladed E779A			5-bladed RDT			
	K_T	$10K_Q$	η_0	K_{TP}	K_{TD}	$10K_Q$	η_0
J = 0.3	0.416	0.708	0.281	0.326	0.177	0.714	0.337
EFD	0.430	0.707	0.290	–	–	–	–
J = 0.6	0.278	0.509	0.522	0.278	0.071	0.630	0.530
EFD	0.285	0.500	0.544	–	–	–	–

However, there is no publicly available noise test data for the E779A propeller. To verify the level of noise performance prediction, the pressure pulsation results of the P-FWH method were compared with the published studies (Ianniello et al., 2013; Sezen et al., 2021b). The comparison results are shown in Figure 3. The results demonstrate that the numerical prediction results of the present study are in better agreement with those of the published studies.

As no experimental measurements were performed on the designed RDT, the uncertainty analysis of the RDT of this study was carried out by two grid schemes with the same distribution and different densities as the reference grid with the refinement ratio $r_G = \sqrt{2}$. A total of three grid schemes were employed, utilizing the Correction Factor method (ITTC, 2021) and the Grid Convergence Index method (ASME, 2021), for the working conditions of the RDT of the present study with the advance coefficient J = 0.6 and the rotational speed n = 1 500 r/min. Table 3 pres-

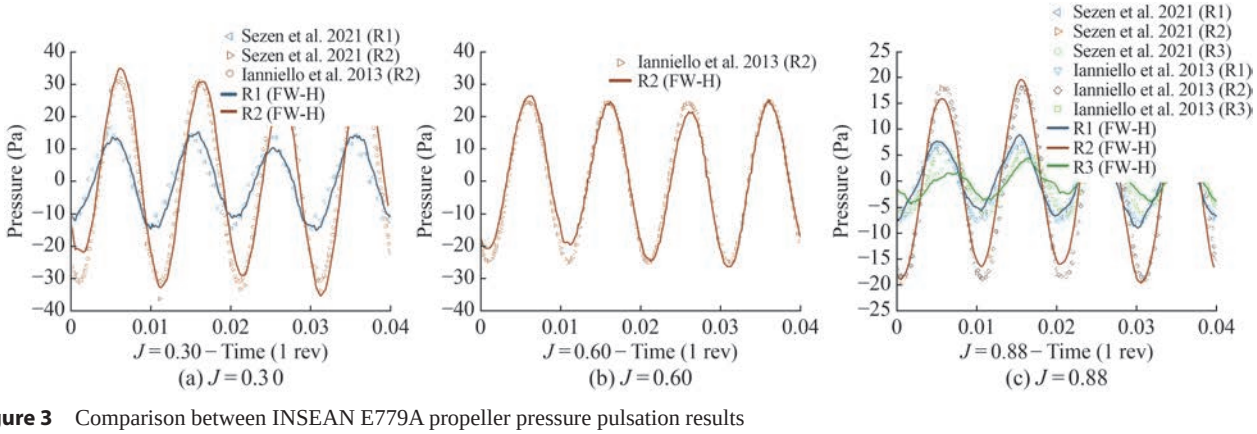

Figure 3 Comparison between INSEAN E779A propeller pressure pulsation results

Table 3 Grid scheme and uncertainty analysis for the rim-driven thruster (J = 0.6, n=1 500 r/min)

Grid schemes					Coarse	Reference			Fine
Cells (mill.)					8.52	21.04			53.51
	Correction factor method				Grid convergence index method				
	R_G	P_G	C_G	U_{SN} (%S_1)	P	e_{21} (%)	e_{32} (%)	GCI_{21} (%)	GCI_{32} (%)
$10K_Q$	0.20	2.30	3.91	0.23	4.59	0.25	1.20	0.08	0.38
K_{TD}	0.59	0.77	0.70	0.08	1.54	1.20	2.09	2.13	3.71
K_{TP}	0.03	4.88	28.48	2.01	9.76	0.04	1.23	0.00	0.05

ents the following information: R_G is the rate of convergence, P_G and P are the order of accuracy, C_G is the correction factor, U_{SN} is the numerical uncertainty, e is the dimensionless form of the approximate relative error, and GCI is the grid index of the neighboring grid scheme. The subscripts 1, 2, and 3 for each physical quantity represent the fine, reference, and coarse grid densities, respectively. The uncertainty analysis indicates that the U_{SN} is less than 3% and that the GCI_{21} is less than GCI_{32} and less than 4%. This suggests that the numerical prediction method employed in this paper is more accurate and reliable.

The results of comparisons with publicly available data and the results of the uncertainty analysis, along with considerations of computational cost, informed the decision to conduct subsequent studies using the reference grid.

3 Results and discussion

3.1 Noise characteristic

Linear spectral noise is generated by the rotational motion of the propeller while subjected to the periodic force of the water flow. This includes thickness noise with monopole characteristics, loading noise with dipole characteristics, and nonlinear turbulence noise with quadrupole characteristics. In contrast, broadband noise is caused by the stochastic change of propeller loading due to propeller-turbulence interaction. This study examines the line-spectrum noise of marine propellers by focusing on the thickness, loading, and turbulence terms in the FW-H equations and comparing two categories of the FW-H method. Additionally, the structural differences between an RDT thruster and a conventional propeller result in a more complex noise source. Consequently, the control of radiated noise and the reduction of acoustic characteristics of the RDT will become a crucial factor in the advancement of rim-driven technology. The conclusions of the study will serve as a valuable reference point.

In this study, the propeller speeds are 1 500 r/min, and the blade passing frequency (BPF) of the E779A propeller is 100 Hz, while the BPF of the five-bladed RDT is 125 Hz. In the previous study, the noise energy is concentrated in the first five harmonics, with the BPF serving as the fundamental frequency. Therefore, it is necessary to cover the range from 0 to 625 Hz. Consequently, the design solutions were analyzed in the frequency range of 2.5 kHz, which encompasses the entire frequency band. In the SPL spectrogram, the blue line is used in this paper to indicate the forecast value calculated by the S-FWH method for impermeable surfaces, the green line is used to indicate the forecast value calculated by the P-FWH method for permeable surfaces, and axial passing frequency (APF) of 25 Hz (in orange) and the BPF and its first-tenth-order harmonic frequency (in pink) are color-marked at the same time.

3.1.1 Thickness noise

The linear thickness noise is generated by the density change of the fluid due to the periodic rotational motion of the blade. Since the P-FWH method integrates over the permeable surface, the monopole term becomes a "pseudo-monopole" term containing a quadrupole contribution, which leads to the discrepancy between the results of the P-FWH method and the S-FWH method.

The results of the E779A propeller thickness noise under heavy-loaded (J = 0.3) and light-loaded (J = 0.6) conditions (Figure 4) indicate that the SPL at the APF for all three receivers exhibits a similar trend. The points of the P-FWH method exhibit a gradually increasing trend ($SPL_{R1} < SPL_{R2} < SPL_{R3}$), whereas the SPL at the APF in the S-FWH method are $SPL_{R3} < SPL_{R1} < SPL_{R2}$. The SPL at the BPF of both the P-FWH and S-FWH methods exhibit an increasing and then decreasing trend ($SPL_{R3} < SPL_{R1} < SPL_{R2}$).

In the case of a heavy-loaded condition, the SPL of the E779A propeller using the P-FWH method is 25 dB higher than that of the S-FWH method at the APF of R1 and R2, and 33 dB higher than that of the S-FWH method at R3. Conversely, under a light-loaded condition, the difference in SPL is reduced, but the difference remains above 6 dB. The discrepancy between the prediction of the SPL at the BPF of the distinct methodologies for R1 and R2 under the light-loaded condition is approximately 4.5 dB, while the divergence in the SPL at R3 is 10.22 dB. This is due to the interference of nonlinear noise, which impairs the ability

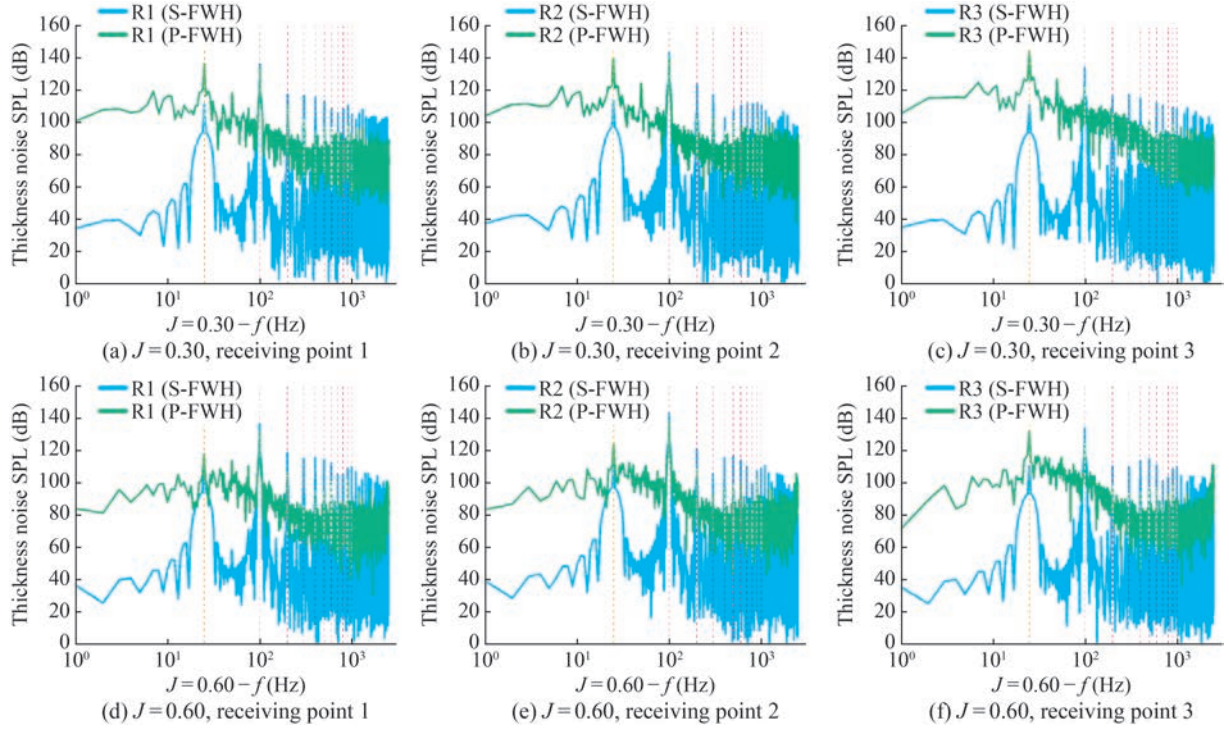

Figure 4 Thickness noise spectrum predicted by S-FWH and P-FWH methods for the E779A propeller

to distinguish the peak frequency, particularly at the receiving point R3. The SPL predicted by different methods at each order harmonic of the R3 have a difference of 10 dB to 20 dB, especially at the 4th-order and 10th-order order harmonics, which are 20.13 dB and 22.70 dB, and at the 9th-order harmonic, which is a smaller difference of 9.12 dB.

Compared with the S-FWH method, the overall SPL of the thickness noise of the E779A propeller using the P-FWH method is 5.64 dB lower at R1, 6.92 dB higher at R2, and 1.23 dB higher at R3 for the heavy-loaded condition, and 1.87 dB lower at R1, 2.30 dB higher at R2, and 8.90 dB lower at R3 for the light-loaded condition.

On the other hand, the RDT has more significant differences in thickness noise levels due to the reflection and transmission from the duct and the unique structure of the rim that affects its sound propagation (Figure 5). Under both heavy-loaded and light-loaded conditions, the SPL at the APF of the three receiving points of the P-FWH method show an increasing trend ($SPL_{R1} < SPL_{R2} < SPL_{R3}$) with smaller differences (4 dB to 6 dB), while the S-FWH method shows a flat trend with smaller differences, with a difference of 1 dB or less. The SPL at the BPF of the three receiving points of the P-FWH and S-FWH methods both show an increasing trend and then a decreasing trend. For the P-FWH method, $SPL_{R3} < SPL_{R1} < SPL_{R2}$ at the BPF, and the SPL at the neighboring receiving points are within 6.5 dB of each other. For the S-FWH method, $SPL_{R1} < SPL_{R3} < SPL_{R2}$ at the BPF, and the difference in SPL at the neighboring receiving points is more than 9 dB.

Under the heavy-loaded condition, the SPL of the RDT using the P-FWH method are higher than those of the S-FWH method by 36.43 dB, 39.76 dB, and 45.16 dB at the APF of R1, R2, and R3, and the difference also decreases under the light-loaded condition, but the difference in the SPL is still more than 28 dB, which is more significant compared with that of the E779A propeller. Furthermore, due to the unique structural differences, the peak prediction at the shaft frequency doubling is more prominent in the SPL spectrum predicted by the RDT under the light-loaded condition. The differences between the P-FWH method and the S-FWH method in the prediction of SPL at BPF of R1, R2, and R3 under the heavy-loaded condition are 16.09 dB, 31.05 dB, 27.87 dB. The differences in the prediction of SPL at BPF of R1, R2, and R3 under the light-loaded condition are 23.43 dB, 34.55 dB, and 33.78 dB.

Compared with the S-FWH method, the overall SPL of thickness noise of the RDT using the P-FWH method is lower by 5.56 dB at the R1 receiving point, 3.46 dB at R2, and 11.39 dB at R3 for the heavy-loaded condition, and lower by 0.62 dB at R1, 12.22 dB at R2, and 21.10 dB at R3 for the light-loaded condition. For the P-FWH method, the thickness noise overall SPL of the E779A propeller is 8.30 dB higher than the RDT at the R1, 11.38 dB higher at the R2, and 8.37 dB higher at the R3 for the heavy-loaded condition. 6.51 dB higher at the R1, 15.66 dB higher at the R2, and 7.76 dB higher at the R3 for the light-loaded condition. For the S-FWH method, the thickness noise overall SPL of the E779A propeller was 1.00 dB higher than that of

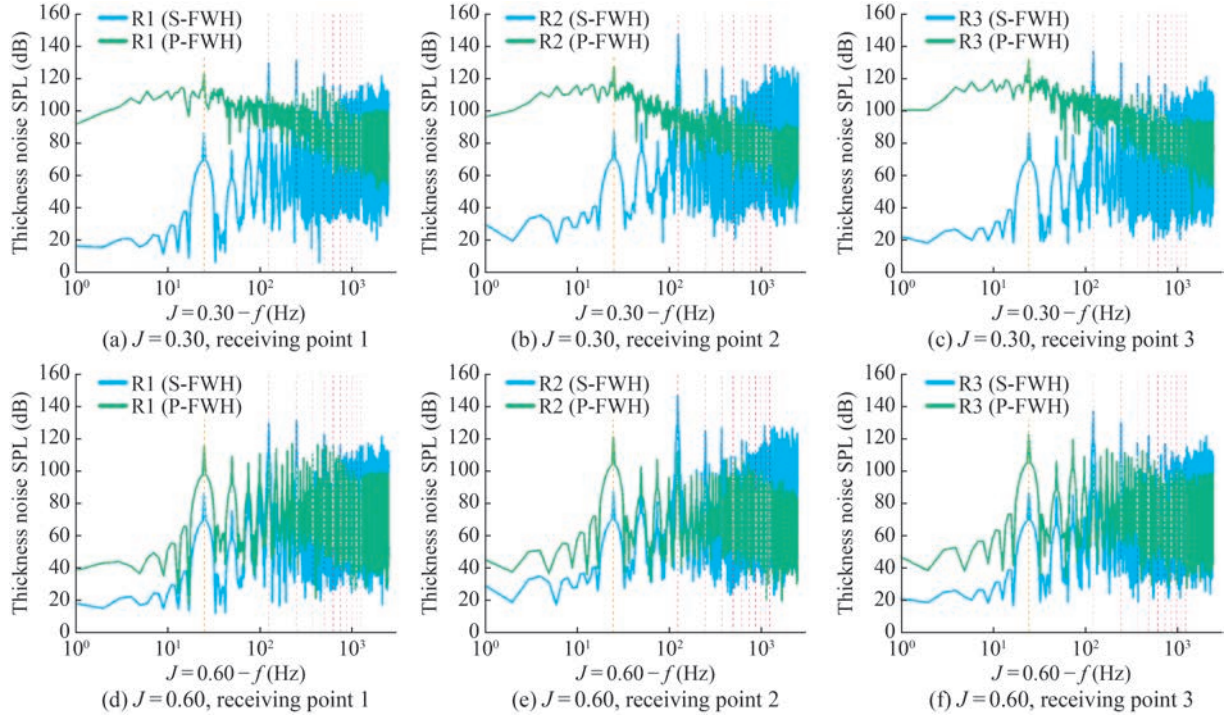

Figure 5 Thickness noise spectrum predicted by S-FWH and P-FWH methods for the rim-driven thruster (a–c for J = 0.3 condition, d–f for J = 0.6 condition)

the RDT at the R1, 4.25 dB lower at the R2, and 4.39 dB lower at the R3 for the heavy-loaded condition, 1.14 dB higher at the R1, 4.44 dB lower at the R2, and 4.36 dB lower at the R3 for the light-loaded condition. Moreover, the contribution of the quadrupole term to the monopole term in the prediction results of the P-FWH method for the RDT is more pronounced in the low-frequency range. The thickness noise of the RDT is markedly less pronounced than that of the E779A propeller in the frequency range below 500 Hz, including at the shaft and blade frequencies. Conversely, the thickness noise of the RDT is more pronounced than that of the E779A in the frequency range above 500 Hz. A propeller in the frequency range exceeding 500 Hz, including the higher-order harmonics, at the three receiving points (R1, R2, and R3) under both heavy- and light-load conditions was observed. The discrepancy between the RDT and E779A in the frequency range exceeding 500 Hz diminished as the load decreased.

3.1.2 Loading noise

Linear loading noise is generated by unsteady forces of the fluid acting on the propeller surface, such as lift and drag, etc. Similarly, the P-FWH method changes the dipole term into a "pseudo-dipole term" containing quadrupole contributions. The loading noise prediction results of the two methods demonstrate a high degree of concordance in the low-frequency region. However, a notable disparity emerges in the high-frequency region, which suggests that the influence of the quadrupole contribution on the dipole term is primarily observed in the high-frequency region.

In this study, in the results of E779A propeller loading noise under heavy-loaded and light-loaded conditions (Figure 6), under the heavy-loaded condition, the SPL of the E779A propeller using the P-FWH method is 16.83 dB higher than that of the S-FWH method at the APF of R1, 19.24 dB higher than that of R2, and 25.47 dB higher than that of R3, and this difference decreases in the light-loaded condition, but the difference in the SPL is still more than 6 dB. The changes in the SPL of the R3 at all harmonics predicted by different methods are larger, especially at the 6th-order harmonics, with a difference of 9.29 dB. The SPL predicted by different methods at each order harmonic of the R3 also vary significantly, especially at the 2nd-order and 5th-order harmonics with a difference of 27.75 dB and 21.96 dB, and at the 8th-order and 10th-order harmonics with a smaller difference of 4.09 dB and 8.60 dB, respectively.

Compared with the S-FWH method, the overall SPL of the loading noise of the E779A propeller using the P-FWH method is 8.25 dB lower at R1, 4.32 dB higher at R2, and 0.40 dB higher at R3 for the heavy-loaded condition, and 2.52 dB lower at R1, 2.10 dB higher at R2, and 9.47 dB lower at R3 for the light-loaded condition.

The loading noise results of the RDT are shown in Figure 7. Under the heavy-loaded condition, the RDT using the P-FWH method is 5.72 dB higher than the S-FWH method at the APF of R1, 10.04 dB higher than the S-FWH method at R2, and 13.96 dB higher than the S-FWH method at R3. Under the light-loaded condition, the P-FWH method

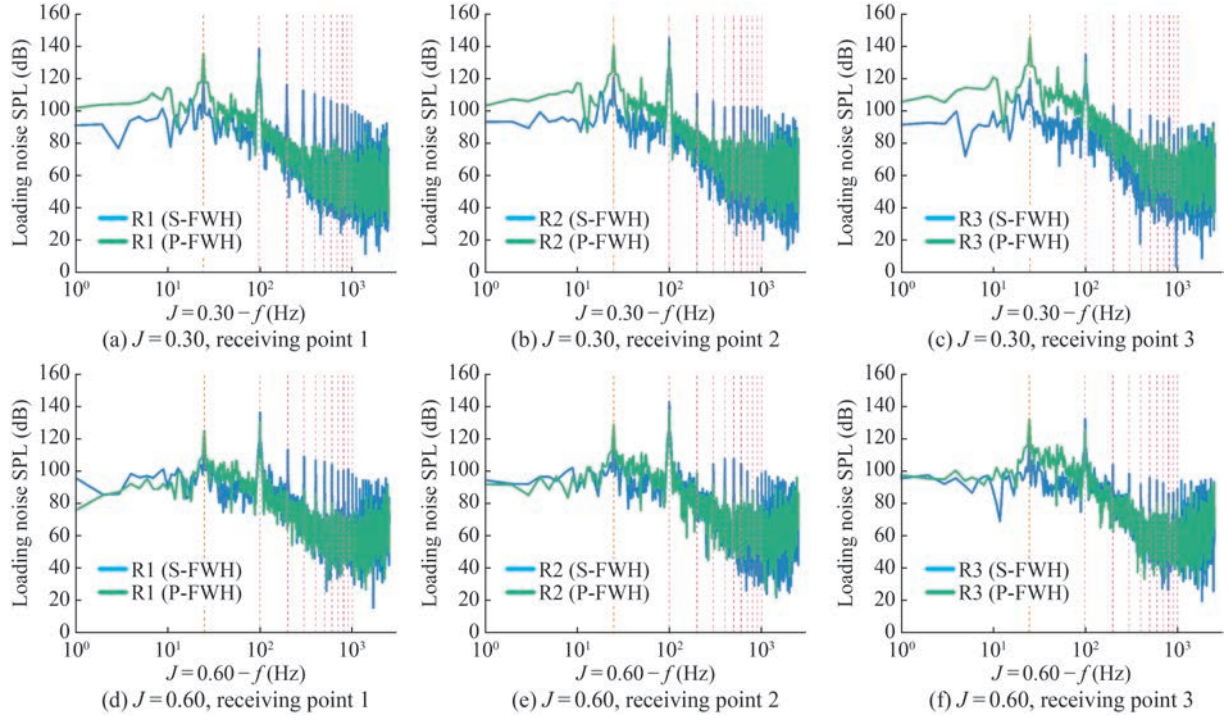

Figure 6 Loading noise spectrum predicted by S-FWH and P-FWH methods for the E779A propeller (a–c for J = 0.3 condition, d–f for J = 0.6 condition)

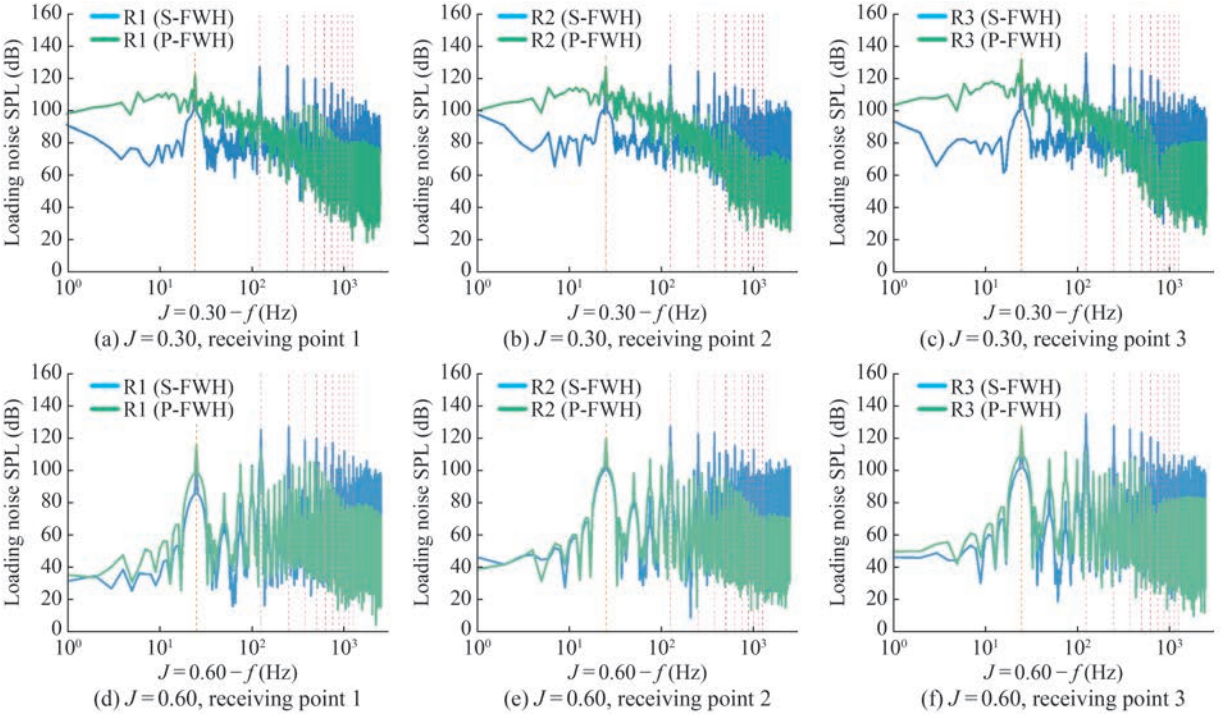

Figure 7 Loading noise spectrum predicted by S-FWH and P-FWH methods for the rim-driven thruster (a–c for J = 0.3 condition, d–f for J = 0.6 condition)

is 12.91 dB higher than the S-FWH method at the APF of R1, 2.48 dB higher than the S-FWH method at R2, and 7.42 dB higher than the S-FWH method at R3. The P-FWH method incorporates a nonlinear noise contribution, which results in a more pronounced difference being observed at the harmonics. Furthermore, the loading noise is affected more significantly at the harmonics than the difference in thickness noise. Additionally, the prominence of the P-FWH

method in loading noise prediction is weaker at the peak frequencies at the harmonics, particularly at the R3 receiving point. Based on the results, it can be seen that, compared with the E779A propeller, the RDT loading noise suffers from a more significant interference at the harmonic frequencies.

Compared with the S-FWH method, the overall SPL of the loading noise of the RDT using the P-FWH method is 8.19 dB lower at R1, 1.56 dB lower at R2, and 3.27 dB higher at R3 for the heavy-loaded condition, 7.70 dB lower at R1, 9.42 dB lower at R2, and 3.85 dB lower at R3 for the light-loaded condition. Furthermore, the quadrupole term contribution to the dipole term in the forecast results of the P-FWH method is predominantly observed in the high-frequency region.

For the P-FWH method, the overall SPL of the loading noise of the E779A propeller is 11.36 dB higher than the RDT at the R1 receiving point, 13.25 dB higher at the R2 receiving point, and 11.42 dB higher at the R3 receiving point for the heavy-loaded condition. For the light-loaded condition, the overall SPL of the loading noise is 12.42 dB higher at the R1, 17.45 dB higher at the R2, and 7.25 dB higher at the R3. For the S-FWH method, the loading noise overall SPL of the E779A propeller is 7.37 dB higher than that of the RDT at the R1, 14.29 dB higher at the R2, and 1.75 dB lower at the R3 for the heavy-loaded condition, 5.93 dB higher at the R1, 12.86 dB higher at the R2, and 3.60 dB lower at the R3 for the light-loaded condition. The loading noise of the RDT is markedly less pronounced than that of the E779A propeller in the frequency range below 500 Hz, including at the shaft and blade frequencies. Conversely, the loading noise of the RDT is more pronounced than that of the E779A in the frequency range above 500 Hz. A propeller in the frequency range exceeding 500 Hz, including the higher-order harmonics, at the three receiving points (R1, R2, and R3) under both heavy- and light-load conditions was observed. The discrepancy between the RDT and E779A in the frequency range exceeding 500 Hz diminished as the load decreased.

3.1.3 Turbulence noise

Nonlinear turbulence noise is caused by the momentum pulsation rate in the fluid, which has a significant effect only when the blade tip operating conditions are transonic or supersonic. In marine propellers, the noise is mainly contributed by the loading noise, and the contribution of quadrupole noise is usually ignored in the noise performance evaluation of marine propellers because the quadrupole noise decays faster and contributes mainly in the near-field region. In this study, a volume integration approach was employed to predict the performance of the quadrupole term noise for the two categories of FW-H (Figures 8 and 9). As illustrated in the figures, the prediction results of the P-FWH and S-FWH methods for the quadrupole term exhibited a high degree of consistency.

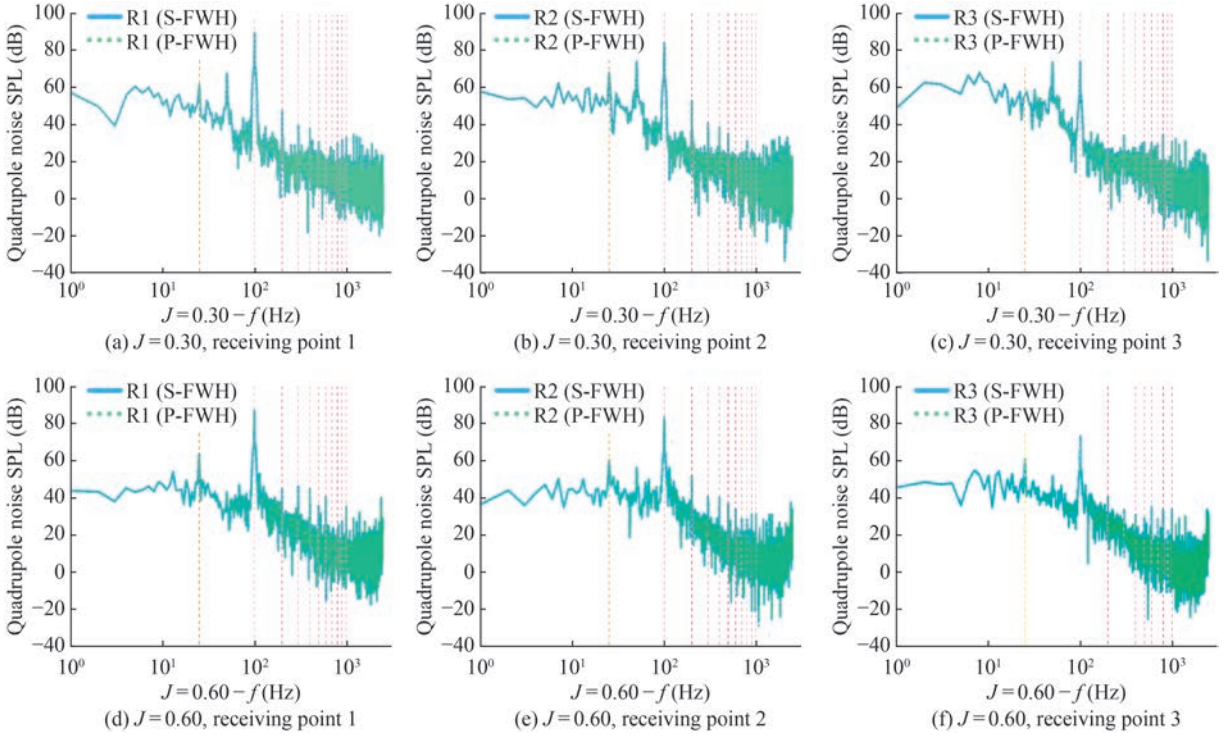

Figure 8 Turbulence noise spectrum predicted by S-FWH and P-FWH methods for the E779A propeller (a–c for J = 0.3 condition, d–f for J = 0.6 condition)

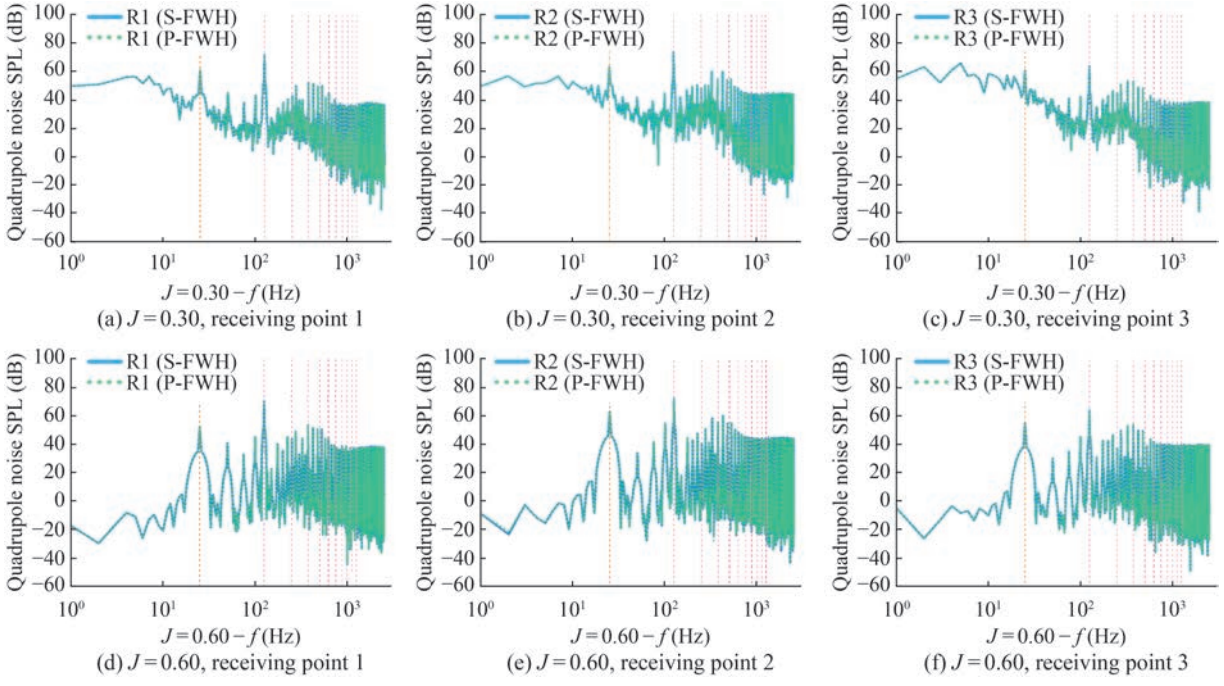

Figure 9 Turbulence noise spectrum predicted by S-FWH and P-FWH methods for the rim-driven thruster (a–c for J = 0.3 condition, d–f for J = 0.6 condition)

In this study, in the results of E779A propeller loading noise under heavy-loaded and light-loaded conditions (Figure 8). Compared with the S-FWH method, the overall SPL of the turbulence noise of the E779A propeller using the P-FWH method is 10.52 dB higher at R1, 4.96 dB lower at R2, and 5.57 dB lower at R3 for the heavy-loaded condition, and 12.90 dB higher at R1, 3.52 dB lower at R2, and 9.38 dB lower at R3 for the light-loaded condition.

The turbulence noise results for the RDT are shown in Figure 9. The P-FWH and S-FWH methods demonstrate a high degree of concordance in their capacity to predict the quadrupole term. Compared with the S-FWH method, the overall SPL of turbulence noise of the RDT using the P-FWH method is higher by 0.71 dB at R1, higher by 1.91 dB at R2, and lower by 2.63 dB at R3 for the heavy-loaded condition, and higher by 4.35 dB at R1, higher by 3.51 dB at R2, and lower by 7.86 dB at R3 for the light-loaded condition. For both the P-FWH and S-FWH methods, the turbulence noise overall SPL of the E779A propeller is 16.37 dB higher than that of the RDT at both the R1, 9.50 dB higher at the R2, and 6.56 dB higher at the R3 for the heavy-loaded condition, and 16.18 dB higher at the R1, 9.16 dB higher at the R2, and 7.64 dB higher at the R3 for the light-loaded condition.

3.2 Wake field

In the acoustic analogy method, the pulsating pressure of an unsteady flow field is solved by CFD, which is used as a sound source to calculate the radiated noise of the propeller. The quadrupole term contribution (volume integral term) is generally neglected for marine propellers, so this subsection focuses on the pressure distribution on the integrating surface in the P-FWH method and the S-FWH method. In this study, vortex identification is visualized for the wake evolution of the E779A propeller and the RDT by the Ω criterion (Liu et al., 2016), which takes the value of 0.52. The method is capable of capturing both strong and weak vortices with a low dependence on the threshold value, and it is effective for analyzing the wake vortices.

Figure 10 illustrates the pressure distribution of the E779A propeller with different FW-H methods. It can be observed that the upstream region of the PDS integrating surface in the P-FWH method exhibits a smaller negative pressure value, the propeller disk region exhibits a higher pressure, and the downstream region exhibits a significant pressure variation. A comparison of Figures 10(a) and 10(d) reveal that the negative and positive peak pressure variations in the downstream region are more pronounced in the heavy-loaded condition than in the light-loaded condition. In comparison to the light-loaded condition, the overall SPL is 2.56 dB higher at R1, 2.06 dB higher at R2, and 5.45 dB higher at R3 for the heavy-loaded condition. The noise results align with the source pressure distribution. However, the S-FWH method integrates directly over the surface of the object. As illustrated in Figures 10(b) and 10(e), the pressure distribution of the pressure surface occupies a greater proportion of the blade tip surface area for the heavy-loaded condition, while there is a significant fluctuation at the blade root for the light-loaded condition. The overall SPL is 1.48 dB higher at R1, 0.92 dB higher at

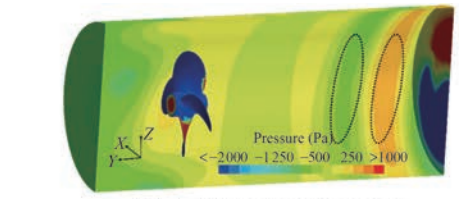

(a) $J = 0.3$, permeable surface

(b) $J = 0.3$, propeller surface

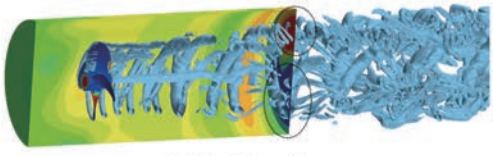

(c) $J = 0.3$, wake vortex

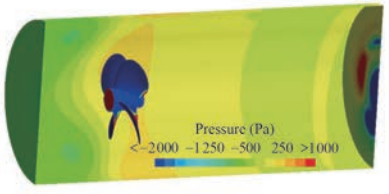

(d) $J = 0.6$, permeable surface

(e) $J = 0.6$, propeller surface

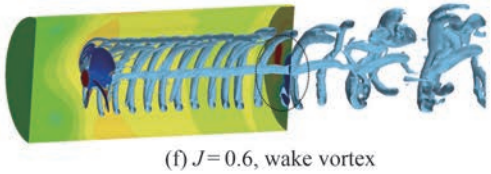

(f) $J = 0.6$, wake vortex

Figure 10 Pressure distribution on the integral surface of the E779A propeller using S-FWH and P-FWH methods

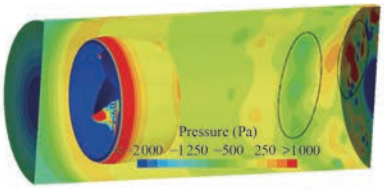

(a) $J = 0.3$, permeable surface

(b) $J = 0.3$, RDT surface

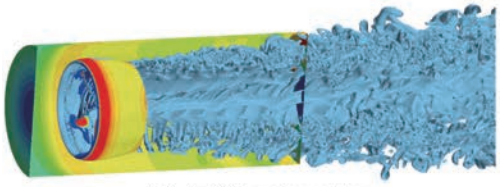

(c) $J = 0.3$, wake vortex

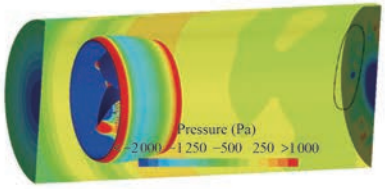

(d) $J = 0.6$, permeable surface

(e) $J = 0.6$, RDT surface

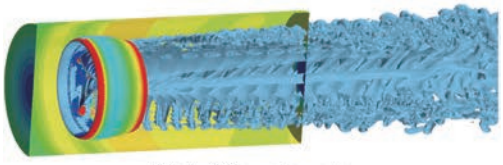

(f) $J = 0.6$, wake vortex

Figure 11 Pressure distribution on the integral surface of the rim-driven thruster using S-FWH and P-FWH methods

R2, and 0.65 dB higher at R3 for the heavy-loaded condition compared to the light-loaded condition.

The pressure distribution of the RDT using different FW-H categories is shown in Figure 11. It can be observed that the pressure in the region of the PDS integrating surface for the P-FWH approach shows the same distribution as the E779A propeller. While at the axial position, the closer the PDS integration surface of the RDT is to the axial position, the lower the pressure is. In addition, the pressure distribution at the downstream end of the PDS integrating surface is significantly different from that of the E779A propeller. The pressure is higher at the leading and trailing edges of the RDT duct surface. Comparing the heavy-loaded and light-loaded conditions (Figures 11(a) and 11(d)), it is also observed that the pressure variations are more drastic in the heavy-loaded condition. Compared to the light-loaded condition, the overall SPL is 2.60 dB higher at R1, 5.23 dB higher at R2, and 5.54 dB higher at R3 for the heavy-loaded condition, where the receiving point R2 is directly above the duct, and its SPL value has a large difference compared to the E779A propeller. According to Figures 11(b) and 11(e), it can be observed that the

pressure distribution on the blade suction surface and pressure surface is the same under heavy-loaded and light-loaded conditions when the S-FWH method is used, while the pressure distribution on the surface of the duct has a large difference. Under the heavy-loaded condition, the pressure in the middle of the duct and the pressure at the trailing edge are closer and at a smaller value, and under the light-loaded condition, the middle of the duct is a negative pressure region with a larger negative pressure value, and the pressure at the trailing edge is extremely positive. Compared with the light-loaded condition, the overall SPL is 0.33 dB higher at R1, 0.07 dB higher at R2, and 0.43 dB higher at R3 for the heavy-loaded condition.

The vortex strength of the propeller is considerably more pronounced than that of the rim-driven thruster. Meanwhile, the slicing pressure distribution of the vortex at the tip of the blade is employed to investigate the correlation between vortex and radiated noise (Figure 12). The vortex flow at the blade tip of the E779A propeller and RDT under the heavy-loaded condition and the pressure distribution were obtained by slicing. Eight slicing planes (1–8) were selected to represent the pressure flow field characteristics near the blade tip. The blade tip vortex is comprised of two distinct components: a blade tip leakage vortex and a blade tip separation vortex. Additionally, the blade tip vortex is connected to a blade-shedding vortex. The negative pressure centers observed in the slices indicate the vortex cores at different evolutionary locations. The mean surface pressure of slice 1 was 5.77 kPa higher than that of slice 5, while slice 2 exhibited a mean surface pressure of 5.69 kPa lower than that of slice 6. Slice 3 exhibited a mean surface pressure of 8.49 kPa lower than that of slice 7, while slice 4 exhibited a mean surface pressure of 8.75 kPa lower than that of slice 8. Conversely, the pressures at the vortex core of slice 1 were 14.19 kPa lower than slice 5, slice 2 was 98.43 kPa lower than slice 6, slice 3 was 73.61 kPa lower than slice 7, and slice 4 was 55.80 kPa lower than slice 8.

The pressure near the blade tip of the RDT is slightly lower than that of the E779A propeller at the inception of the blade tip vortex. As the vortex evolves, the pressure near the blade tip is observed to gradually increase in comparison to that of the E779A propeller. The pressure distribution at the vortex core indicates that the intensity of vortex leakage at the blade tip of the RDT is significantly reduced compared to that of the conventional propeller. This reduction in leakage also results in a reduction in noise levels. Figure 13 shows the results of the pulsating pressure monitoring of the blade tip leakage vortex near the blade tip of the propeller. The amplitude of the E779A propeller is found to be greater than that of the RDT in both heavy-loaded and light-loaded conditions. The root-mean-square (RMS) value of the E779A propeller pressure is 287.21 Pa higher than that of the RDT under the heavy-loaded condition. The RMS value of the E779A propeller pressure is higher than that of the RDT by 622.90 Pa under the light-loaded condition, which further illustrates the effect of the vortex pulsation pressure distribution on the noise performance of the RDT. Moreover, the discrepancies in wake formation resulting from the distinctive design of the RDT necessitate further comprehensive investigation to regulate the noise level at the vortex evolution mechanism.

Furthermore, it can be observed that there is a significant correlation between the permeable integral surfaces

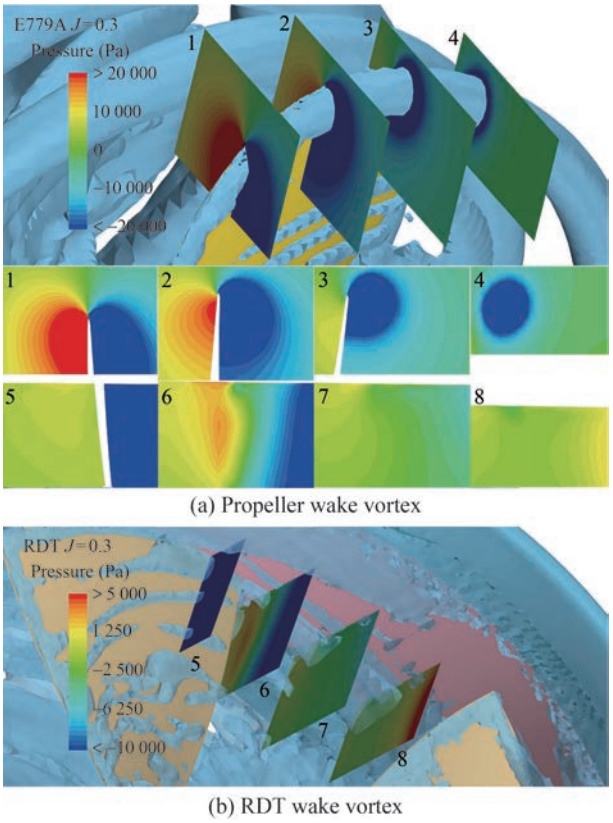

Figure 12 Tip vortex slice and pressure distribution of propeller under $J = 0.3$ condition

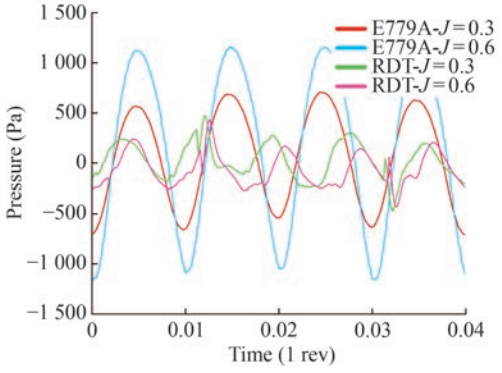

Figure 13 Pulsation pressure near the tip of the blade (coordinates of the receiving point: $[X = 0, Y = -0.5R, Z = 0.9R]$)

depicted in Figures 10 and 11 and the evolution process of the thruster wake vortex(Felli et al., 2006, 2011). As illustrated in Figures 6 and 7, there is a notable degree of signal overlap between the P-FWH and S-FWH methods under varying loading conditions (J = 0.3 & 0.6). Furthermore, Figure 13 demonstrates a significant disparity in the pulsation pressure amplitude in the proximity of the thruster under varying loading conditions. This indicates that the local pressure field in the thruster demonstrates variability under different loading conditions. In acoustic analysis, the pulsating pressure serves as a sound source and exerts a direct influence on the SPL spectrum. However, the peak frequencies observed in the SPL spectra of heavy-loaded and light-loaded are found to be nearby, a phenomenon that is deemed unusual and necessitates further investigation to ascertain its underlying causes.

3.3 Numerical pseudo-noise

To accurately calculate the radiated noise of the RDT, it is necessary to investigate the unphysical numerical noise generated by the reflection and slip interface at the boundary of the computational domain, as well as the numerical disturbances such as the pressure correction method. At present, the pseudo-noise problem of the P-FWH method mainly focuses on the slip interface. The slip interface is a widely used technique in numerical simulations of the hydrodynamic performance of rotating machinery. It is employed for transferring pressure, velocity, and other data between static and rotating domains. However, from the perspective of noise generation, this technique may lead to the introduction of additional numerical noise problems, which can result in the contamination of the overall sound pressure, particularly in the far field where pressure fluctuations are minimal. Furthermore, the P-FWH method employs a layer of permeable surfaces to forecast the thruster and its wake computationally. This may also generate additional numerical noise, which can contaminate the overall noise performance.

To address the issue of numerical noise, this study employs a pressure derivation technique to visualize the numerical noise generated at each interface through the pressure-time derivative (James et al., 1977; Sezen et al., 2021a; Siemens, 2022). From basic transport equations, the substantial or material derivative for pressure is:

$$\frac{DP}{Dt} = \frac{\partial P}{\partial t} + \boldsymbol{v} \cdot \nabla P \tag{11}$$

Hence to obtain the pressure derivative in a simulation with mesh motion, it must be calculated:

$$\frac{\partial P}{\partial t} = \frac{DP}{Dt} - \boldsymbol{v} \cdot \nabla P \tag{12}$$

For the moving speed of the mesh, can be calculated from the current time-step and the previous two time-steps in the numerical simulation, as defined below:

$$\boldsymbol{v} = \frac{3X_0 - 4X_1 + X_2}{2\Delta t} \tag{13}$$

where X_0 denotes the current time-step position, X_1 denotes the first previous time-step position, and X_2 denotes the second previous time-step position.

Finally, for the pressure-time derivative, the solution is as follows:

$$\frac{\mathrm{d}P}{\mathrm{d}t} = \frac{3P_0 - 4P_1 + P_2}{2\Delta t} - \boldsymbol{v} \cdot \nabla P \tag{14}$$

where P is the pressure and Δt is the time-step. The pressure difference between consecutive time-steps is calculated using the pressure values stored at each node for the first two time-steps, thus visualizing the change of pressure in the flow field over time.

This study presents a summary of the pressure-time derivative visualization results for the RDT at different grid resolutions (Table 3) for the J = 0.6 condition. The results are presented in Figure 14, which indicates the pressure fluctuations induced at the slip interface. However, there is no source of noise at the slip interface that would cause its pressure to change drastically. Therefore, the pressure fluctuations generated at the intersection interface are evidence of the generation of unphysical numerical noise. Figure 14 presents a comparison of different grid resolutions in this study. It reveals that the pressure fluctuation range at the slip interface is the largest in the coarse grid of Figure 14(a), followed by the reference grid of Figure 14(b). In contrast, the pressure fluctuation range is the smallest in the fine grid of Figure 14(c). This indicates that the numerical noise problem at the slip interface diminishes with the increase of the grid resolution. Consequently, an increase in grid resolution can effectively mitigate the numerical noise problem at the slip interface. The findings of Sezen et al. (Sezen et al., 2021a) also demonstrate that noise pollution can be mitigated by enhancing grid resolution. Furthermore, the enhancement in grid resolution can facilitate the capture of finer flow field features and enhance the accuracy of noise level forecasting. In comparison to the reference grid, the overall SPL (without consideration of volume integration) of the fine grid is 0.97 dB higher at the R1, 6.01 dB higher at the R2, and 9.66 dB higher at the R3. The overall SPL of the coarse grid is 2.11 dB lower at the R1, 5.35 dB lower at the R2, and 7.77 dB lower at the R3. The results of the noise prediction align well with the vortex evolution of the wake field in Figure 14.

In conclusion, the result of the pressure-time derivative to visualize the flow field can observe the generation of

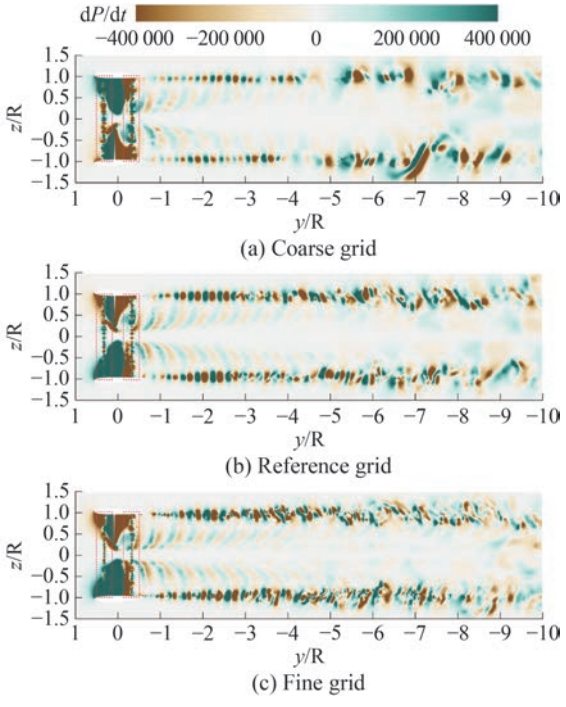

Figure 14 Numerical noise visualization results induced by different grid resolutions at $J = 0.6$

numerical noise. Therefore, the pressure-time derivative is an effective technical tool for observing numerical noise contamination. In addition, significant numerical noise contamination is observed at the slip interface, while no significant numerical noise is observed at the permeable surface region. This is due to the motion of the slip interface resulting in its poor mesh transition, while the smooth transition inside and outside the permeable surface reduces its numerical noise generation. Therefore, the mesh transition between the computational domains can be smoothed by adjusting the mesh discretization so that the numerical noise problem caused by the computational domain boundaries can be reduced, but its effect cannot be eliminated. Further, the noise contamination caused by the slip interface may lead to changes in the fluctuation amplitude and shape of the pulsating pressure signal, which contaminates the prediction of the noise performance. Therefore, how to effectively eliminate noise pollution is a key issue that needs to be studied in depth urgently.

Furthermore, the pressure-time derivative flow field visualization in this study allows for the observation of blade tip leakage vortices and blade shedding vortices at the trailing edge of the RDT, as well as leakage vortices at the blade root tip of the hubless RDT (Figure 15). Consequently, this technique can be employed not only to observe the generation of numerical noise at the interfaces but also to make judgments on the trailing vortices. The current vortex identification technique is not entirely independent of the threshold value, and the second-generation vortex identification methods exhibit varying degrees of vortex expansion according to the selected threshold value. This can result in erroneous judgments regarding the evolution of the vortex. In contrast, the pressure-time derivative technique enables the precise localization and tracking of vortex cores. Thus, the technique can provide reliable corroboration of the thruster wake evolution.

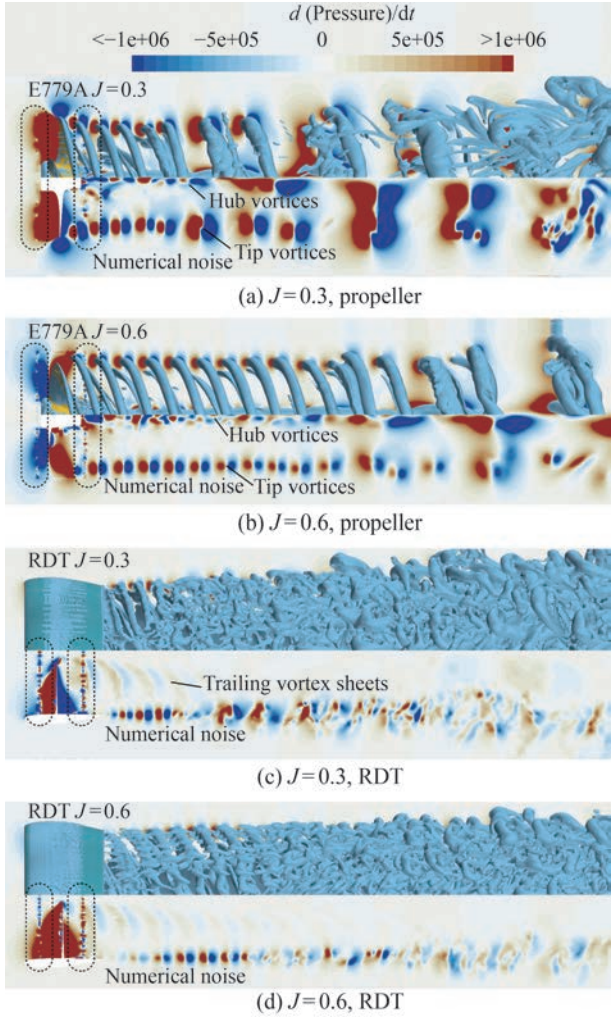

Figure 15 Correlation between the evolution of the thruster wake vortex and the pressure-time derivative

4 Conclusion

This study employs a hybrid method of IDDES and FW-H to characterize the noise of a rim-driven thruster under non-cavitation, uniform flow conditions. The study specifically investigates the rim-driven thruster noise characterization using the E779A propeller as a reference object and compares the prediction results of the two categories in the FW-H method. This comparison explores the differences in thickness noise, loading noise, and turbulence noise under different loading conditions. Furthermore, the discrepan-

cies in noise forecasting between the two categories are elucidated through the pressure distribution (sound source) on the integration surface. Additionally, this study elucidates the numerical noise problem that exists in the P-FWH method through the pressure-time derivative. The findings of this study can serve as a reference for the design of rim-driven thrusters while enriching the research in the field of underwater radiated noise. The following conclusions are drawn from this study:

1) The P-FWH method has been shown to underestimate the thickness noise and loading noise of the rim-driven thruster when compared to the S-FWH method, under differing loading conditions. The effect on the low-frequency monopole and high-frequency dipole is significant.

2) The noise level of the rim-driven thruster is considerably lower than that of the E779A propeller, with a maximum reduction of 21.88 dB observed under different loading conditions.

3) Pressure patterns tie closely to vortex evolution, necessitating a deeper study of vortex dynamics for noise control optimization.

4) Pressure-time derivative visualize numerical noise and track vortex cores, while optimized grids curb noise and enhance flow field prediction accuracy.

In conclusion, despite the presence of numerical noise in the P-FWH method, which may result in alterations to the amplitude or overall shape of the pressure signal, the computational accuracy of the method has been demonstrated to meet the preliminary design requirements for the noise performance of the rim-driven thruster.

Funding The National Natural Science Foundation of China (Grant No. 52201376), and the Natural Science Foundation of Hubei Province, China (Grant No. 2023AFB683).

Competing interest The authors have no competing interests to declare that are relevant to the content of this article.

References

Abu Sharkh SM, Turnock SR, Hughes AW (2003) Design and performance of an electric tip-driven thruster. Proceedings of the Institution of Mechanical Engineers, Part M: Journal of Engineering for the Maritime Environment 217: 133-147. https://doi.org/10.1243/147509003322255840

Andersen S, Andersen P (1987) Hydrodynamic design of propellers with unconventional geometry. Royal Institution of Naval Architects Transactions

ASME (2021) Standard for Verification and Validation in Computational Fluid Dynamics and Heat Transfer

Brentner KS, Farassat F (1998) Analytical comparison of the acoustic analogy and Kirchhoff formulation for moving surfaces. AIAA Journal 36: 1379-1386. https://doi.org/10.2514/2.558

Chen Y, Wang L, Hua HX (2017) Longitudinal vibration and unsteady thrust transmission of the rim driven thruster induced by ingested turbulence. Ocean Eng 131: 149-161. https://doi.org/10.1016/j.oceaneng.2017.01.001

Cruz E, Lloyd T, Lafeber FH, Bosschers J, Vaz G, Djavidnia S (2022) The SOUNDS project: towards effective mitigation of underwater noise from shipping in Europe, in: Proceedings of Meetings on Acoustics. 22nd International Symposium on Nonlinear Acoustics, Oxford, UK, 070021. https://doi.org/10.1121/2.0001638

Di Francescantonio P (1997) A new boundary integral formulation for the prediction of sound radiation. J Sound Vibration 202: 491-509. https://doi.org/10.1006/jsvi.1996.0843

Duarte CM, Chapuis L, Collin SP, Costa DP, Devassy RP, Eguiluz VM, Erbe C, Gordon TAC, Halpern BS, Harding HR, Havlik MN, Meekan M, Merchant ND, Miksis-Olds JL, Parsons M, Predragovic M, Radford AN, Radford CA, Simpson SD, Slabbekoorn H, Staaterman E, Van Opzeeland IC, Winderen J, Zhang X, Juanes F (2021) The soundscape of the anthropocene ocean. Science 371: eaba4658. https://doi.org/10.1126/science.aba4658

Farassat F (2007) Derivation of Formulations 1 and 1A of Farassat (No. Nasa/TM-2007214853 214853).

Felli M, Di Felice F, Guj G, Camussi R (2006) Analysis of the propeller wake evolution by pressure and velocity phase measurements. Exp. Fluids 41: 441-451. https://doi.org/10.1007/s00348-006-0171-4

Felli M, Camussi R, Di Felice F (2011) Mechanisms of evolution of the propeller wake in the transition and far fields. J. Fluid Mech 682: 5-53. https://doi.org/10.1017/jfm.2011.150

Ffowcs Williams JE, Hawkings DL (1969) Sound generation by turbulence and surfaces in arbitrary motion. Phil. Trans. R. Soc. Lond. A 264: 321-342. https://doi.org/10.1098/rsta.1969.0031

Gaggero S, Gonzalez-Adalid J, Perez Sobrino M (2016a) Design of contracted and tip loaded propellers by using boundary element methods and optimization algorithms. Appl. Ocean Res 55: 102-129. https://doi.org/10.1016/j.apor.2015.12.004

Gaggero S, Gonzalez-Adalid J, Sobrino MP (2016b) Design and analysis of a new generation of CLT propellers. Appl. Ocean Res 59: 424-450. https://doi.org/10.1016/j.apor.2016.06.014

Gaggero S (2023) A study on the wake evolution of a set of rim-driven thrusters. JMSE 11: 1659. https://doi.org/10.3390/jmse11091659

Ge M, Svennberg U, Bensow RE (2022) Investigations on prediction of ship noise using the FWH acoustic analogy with incompressible flow input. Ocean Eng 257: 111531. https://doi.org/10.1016/j.oceaneng.2022.111531

Gong J, Ding J, Wang L (2021) Propeller–duct interaction on the wake dynamics of a ducted propeller. Phys. Fluids 33: 074102. https://doi.org/10.1063/5.0056383

Gong J, Guo C, Zhao D, Wu T, Song K (2018) A comparative DES study of wake vortex evolution for ducted and non-ducted propellers. Ocean Eng 160: 78-93. https://doi.org/10.1016/j.oceaneng.2018.04.054

Gong J, Wu Z, Ding J (2023) Numerical analysis on the transom-stern wake with a horizontal plunging jet. Ocean Eng 285: 115465. https://doi.org/10.1016/j.oceaneng.2023.115465

Hughes AW, Sharkh SA, Turnock SR (2000) Design and testing of a novel electromagnetic tip-driven thruster. The Tenth International Offshore and Polar Engineering Conference, OnePetro, ISOPE-I-00-153

Ianniello S, Muscari R, Di Mascio A (2013) Ship underwater noise assessment by the acoustic analogy. Part I: nonlinear analysis of a marine propeller in a uniform flow. J. Mar. Sci. Technol 18: 547-570. https://doi.org/10.1007/s00773-013-0227-0

ITTC (2021) ITTC Quality System Manual Recommended Procedures:

Uncertainty Analysis in CFD Verification and Validation, Methodology and Procedures. The 29th International Towing Tank Conference, Virtual, Online

ITTC (2014a) Specialist Committee on Hydrodynamic Noise Final Report and Recommendations to the 27th ITTC. 27th International Towing Tank Conference, Copenhagen, Denmark

ITTC (2014b) ITTC Quality System Manual Recommended Guidelines: Practical Guidelines for Ship CFD Applications. 27th International Towing Tank Conference, Copenhagen, Denmark

James ML, Smith GM, Wolford JC (1977) Applied numerical methods for digital computation with FORTRAN and CSMP, 2nd ed. IEP, New York

Lea M, Thompson D, Blarcom B, Eaton J, Friesch J, Richards J (2003) Scale model testing of a commercial rim-driven propulsor pod. Journal of Ship Production 19: 121-130. https://doi.org/10.5957/jsp.2003.19.2.121

Lidtke AK, Lloyd T, Vaz G (2019) Acoustic modelling of a propeller subject to non-uniform inflow, in: Sixth International Symposium on Marine Propulsors, SMP2019. Sixth International Symposium on Marine Propulsors, Rome, Italy

Liu C, Wang Y, Yang Y, Duan Z (2016) New omega vortex identification method. Sci. China Phys. Mech. Astron 59: 684711. https://doi.org/10.1007/s11433-016-0022-6

Lloyda TP, Lidtke AK, Rijpkema DR, van Wijngaarden E, Turnock SR, Humphrey V (2015) Using the FW-H equation for hydroacoustics of propellers, in: 15th Numerical Towing Tank Symposium. 15th Numerical Towing Tank Symposium, Cortona, Italy

Sezen S, Atlar M (2023) Marine propeller underwater radiated noise prediction with the FWH acoustic analogy Part 1: Assessment of model scale propeller hydroacoustic performance under uniform and inclined flow conditions. Ocean Eng 279: 114552. https://doi.org/10.1016/j.oceaneng.2023.114552

Sezen S, Cosgun T, Yurtseven A, Atlar M (2021a) Numerical investigation of marine propeller Underwater Radiated Noise using acoustic analogy part 1: The influence of grid resolution. Ocean Eng 220: 108448. https://doi.org/10.1016/j.oceaneng.2020.108448

Sezen S, Cosgun T, Yurtseven A, Atlar M (2021b) Numerical investigation of marine propeller underwater radiated noise using acoustic analogy. Part 2: The influence of eddy viscosity turbulence models. Ocean Eng 220: 108353. https://doi.org/10.1016/j.oceaneng.2020.108353

Sharma S, Jesudhas V, Balachandar R, Barron R (2019) Turbulence structure of a counter-flowing wall jet. Physics of Fluids 31: 025110. https://doi.org/10.1063/1.5082550

Shur ML, Spalart PR, Strelets MKh, Travin AK (2008) A hybrid RANS-LES approach with delayed-DES and wall-modelled LES capabilities. Int. J. Heat Fluid Flow 29: 1638-1649. https://doi.org/10.1016/j.ijheatfluidflow.2008.07.001

Siemens (2022) Theory Guide for STAR-CCM+17.06

Sørensen PM, Haddock A, Guarino E, Jaakkola K, McMullen C, Jensen FH, Tyack PL, King SL (2023) Anthropogenic noise impairs cooperation in bottlenose dolphins. Current Biology 33: 749-754.e4. https://doi.org/10.1016/j.cub.2022.12.063

Spalart PR (2009) Detached-eddy simulation. Annu Rev Fluid Mech 41: 181-202. https://doi.org/10.1146/annurev.fluid.010908.165130

Spalart PR, Jou WH, Strelets MK, Allmaras SR (1997) Comments on the feasibility of LES for wings and on a hybrid RANS/LES approach, in: Advances in DNS/LES, 4-8

Tan W, Yan X, Liu Z, Zhang C, Huang Q, Tian Z (2015) Technology development and prospect of shaftless rim-driven propulsion system. Journal of Wuhan University of Technology (TSE) 39(3): 601-605

Testa C, Porcacchia F, Zaghi S, Gennaretti M (2021) Study of a FWH-based permeable-surface formulation for propeller hydroacoustics. Ocean Eng 240: 109828. https://doi.org/10.1016/j.oceaneng.2021.109828

Transport Canada/Government of Canada (2019) Quieting Ships to Protect the Marine Environment Workshop Final Report (No. Acentech Project No. 630964)

Wang L, Wu T, Gong J, Yang Y (2021) Numerical analysis of the wake dynamics of a propeller. Phys. Fluids 33: 095120. https://doi.org/10.1063/5.0064100

Wu Z, Gong J, Ding J, Sun Y, Ma C (2023a) Autonomous modification and optimization method for rim-driven system in surface ships. Ocean Eng 290: 116293. https://doi.org/10.1016/j.oceaneng.2023.116293

Wu Z, Gong J, Ding J, Zhang D (2023b) Parametric design and optimization method for forward and reverse equal-thrust shaftless rim-driven thruster blades. In: The 34th National Conference on Hydrodynamics. Ningbo University, China, 1515-1525

Yan X, Liang X, Ouyang W, Liu Z, Liu B, Lan J (2017) A review of progress and applications of ship shaft-less rim-driven thrusters. Ocean Eng 144: 142-156. https://doi.org/10.1016/j.oceaneng.2017.08.045